Finite Element simulation of hydrogen transport during plastic bulging of iron submitted to gaseous hydrogen pressure

Yann Charles, Monique Gaspérini, Nicolas Fagnon, Kevin Ardon, Anthony Duhamel

Finite Element simulation of hydrogen transport during plastic bulging of iron submitted to gaseous hydrogen pressure

Yann CHARLES[a,1], Monique GASPÉRINI[a], Nicolas FAGNON[a], Kevin ARDON[a], Anthony DUHAMEL[a]

a. Université Paris 13, LSPM, CNRS, Paris Sorbonne Cité, 99 avenue JB Clément, F-93430 Villetaneuse, France

Abstract

Disk Pressure Tests on polycrystalline Armco iron flat samples provided fracture pressure values within a wide range of applied hydrogen pressure rise rates. FE simulations of the disk bulging and hydrogen transport before fracture have been performed assuming isotropic elastoplasticity. The diffusive and trapped hydrogen concentrations fields in the zone of interest for failure show the effect of the applied pressure rise rate on the coupling between plastic strain and hydrogen transport, and permit to deduce a phenomenological relationship between the failure stress and the hydrogen concentration, as a first approximation to model the embrittlement process. Submodelling with 3D synthetic polycrystals, obeying crystal plasticity, permits to exhibit statistically the effects of local heterogeneities on the hydrogen distribution, and their consequences on the phenomenological failure stress evolution with the hydrogen content.

Keywords: Hydrogen; diffusion; trapping; finite elements; crystal plasticity

Nomenclature

C_L: diffusive hydrogen concentration

C_T: trapped hydrogen concentration

C_0: normalization hydrogen concentration

ε_p: equivalent plastic strain

P_F: failure pressure

$\dot{P}$: pressure rate

σ_{Prin}: principal stress (max σ_{Prin}: maximal principal stress)

σ_R: failure stress

$\langle X \rangle$: mean value for X

Acronyms

DPT: Disk Pressure Test

HE: Hydrogen embrittlement

SEM: Scanning Electron Microscopy

ZoI: Zone of Interest

[1] Corresponding author, yann.charles@univ-paris13.fr, tel: (33) 1 49 40 34 61, fax: (33) 1 49 40 39 38

1 Introduction

Hydrogen embrittlement (HE) is a severe risk of failure of metallic structures, especially for hydrogen transportation and storage. In the context of sheet metal forming, HE may occur during complex mechanical loading, due to the concomitant effect of the macroscopic boundary conditions, anisotropic crystal plasticity, and local heterogeneities. Hydrogen transport, assisted by stress fields and hindered by trapping by dislocations [1], has consequently to be considered at different scales for reliable finite element simulations of the risk of embrittlement.

To study metallic structures reliability while submitted to gaseous hydrogen pressure, the Disk Pressure Test [2] permits to approach realistic conditions with a laboratory test. This specific mechanical test, hereafter called DPT, has been developed to select materials for hydrogen storage applications. In this test, a thin metallic disk is bulged out until fracture by gas pressure. The ratio of failure pressures under H_2 and a neutral gas (usually He) is used as a phenomenological index of HE in technical standardization [3,4]. Beyond this applicative purpose, the DPT is an interesting challenge for numerical simulations, since it is a severe initial and value boundary problem involving simultaneously applied stress boundary conditions, hydrogen transport and trapping, and leading to large plastic strain fields and hydrogen concentration evolution in the same zone of interest. Simulations of such conditions are also interesting to analyze the phenomena of hydrogen induced blistering [5,6], which is one of the experimental evidence of HE, involving local bulging under hydrogen pressure.

In a previous work [2], finite element simulation of the DPT has been proposed, including a hydrogen-dependent cohesive zone approach to describe pressure fracture under hydrogen gas. Computations have been made at the macroscopic level, assuming isotropic standard elastoplasticity and hydrogen standard Fick diffusion, which are very rough approximations both of material behavior and of hydrogen transport. Accounting for stress-driven diffusion and hydrogen trapping by dislocations, the Krom equation [1,7,8] was implemented in Abaqus code to better describe, though phenomenologically, hydrogen-materials interactions, and was successfully applied to high strength steels for hydrogen cylinders [9,10]. Some submodelling attempts have been made in the zone of interest, using virtual microstructures far from being realistic for the considered bainitic material. Moreover, in these works, only one value of applied pressure rise rate was considered, while several characteristic times are expected to interact during disk bulging because of concomitant hydrogen transport and mechanical loading. In the Krom equation, based on Oriani's equilibrium assumption [11], only instantaneous trapping is accounted for, whereas trapping and detrapping kinetics may control the physical hydrogen-material interactions [12]. In a recent work [13,14], transient trapping was implemented in Abaqus code, using an analytical approximation of the McNabb and Foster equation, and was proved to be efficient for 3D simulations [15].

In this context, the objective of this work are (i) to analyze numerically the relative influence of different characteristic times (mechanical loading, diffusion, trapping process) on the hydrogen concentration fields in the disk during its bulging under hydrogen gas, (ii) to propose a phenomenological hydrogen dependent stress-driven criteria for the brittle failure initiation, and (iii) to discuss the effect of material behavior, including the polycrystalline scale.

Armco iron was considered in the study to benefit from hydrogen-related parameters available in the literature for simulations, and to deal with realistic virtual polycrystalline aggregates for single-phase material. Finite element simulations of the DPT have been made up to the experimental pressure values for fracture under hydrogen. Assuming HE by a mode-I fracture,

a relationship is proposed between a critical maximal stress and the mean hydrogen concentration in the zone of interest for fracture in the disk, from inverse identification using experimental fracture pressures in the DPT from various pressure rise rate values.

Computations have been performed first at the macroscopic scale assuming isotropic material behavior, then 3D submodeling on polycrystal aggregates obeying crystal plasticity have been made to analyze statistically the effect of crystal anisotropy on the mechanical and hydrogen concentration fields in the zone of interest (ZoI) for fracture, and the potential consequence for the risk of failure. The paper is organized as follow: first the experimental data are presented, then the most salient equations for hydrogen transport are summarized, followed by the FE simulations at the macroscopic and at the polycrystal scales.

2 Experimental results from DPT and tensile tests

Armco© iron was used for the study. Samples for tensile tests and DPT were cut off from the as-provided annealed cold-rolled sheet of 1 mm thickness.

2.1 DPT tests

Samples for DPT were 55 mm wide. The central zone of the disk with diameter 26.5 mm is submitted to hydrogen pressure, while the outer part is blocked by the clamping device. In the zone of interest for HE, located close to the clamping area, the metal is bent over the upper flange of radius 0.5 mm (see [2] for the general configuration of the test). The DPT tests were performed following the specified procedures [3,4], with a constant applied pressure rise rate $\dot{P}$ in the range [0.001-25 MPa/s]. Figure 1 shows the variation with applied pressure rise rate of the failure pressure P_F during the DPT test under helium or hydrogen gas. Despite a rather low hydrogen sensitivity when referring to the HE index value (around 1.1), which is not surprising for pure iron compared to high strength steels [10,16], the results clearly show a net decrease of the fracture pressure under hydrogen for a large $\dot{P}$ range, typically from 3×10^{-3} to 20 MPa/s.

Fracture always occurred from the same disk area, located in front of the upper flange, which defined the zone of interest (ZoI) for fracture (see below, Figure 4a) – as observed for DPT on other materials [2]. SEM observations of the fracture surfaces confirmed HE occurrence in the disks broken under hydrogen: typical flat areas with brittle-like aspect are presented in Figure 2.

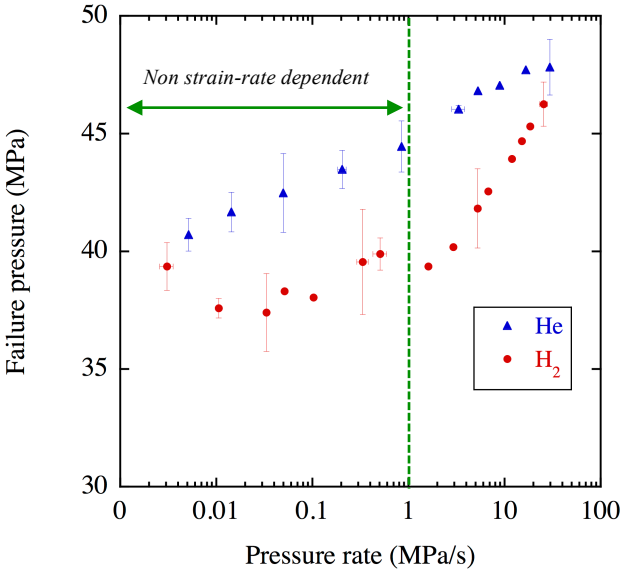

Figure 1. DPT results under He and H_2 gas for selected applied pressure rise rates. The dashed green line point out shows the domain of strain rate-independency according tensile test for strain-rates predicted by FE simulation of the DPT (see Section 3).

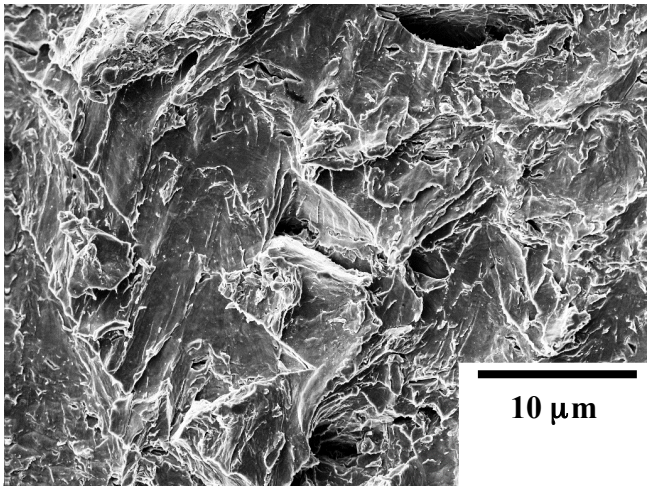

Figure 2. Brittle-like fracture surface of a disk after DPT at 1.5 MPa/s. P_F=40 MPa.

It can be noticed from Figure 1 that HE appears to vanish both for the lowest and the highest $\dot{P}$ values.

For the lowest pressure rates, due to the test duration, contamination of the sample surface by some inherent residual impurities of the gas [17,18] could prevent hydrogen diffusion in the sample bulk, such as the development of a thin oxide layer [19,20] depending on the partial oxygen pressure. This phenomenon needs further investigations, beyond the scope of the present study. On the opposite, at high pressure rates, hydrogen diffusion is expected to be less efficient during the short duration of plastic bulging, consistently with a lowering of HE.

The values of failure pressure under He gas increase roughly linearly with $\dot{P}$ (with a global variation range lower than 20%), suggesting rate effects on the DPT. Such an increase of failure pressure with pressure rate was observed in several works on DPT, for different materials [3,17,21], without any clear link with material viscosity. In all cases, the salient feature of the test is that hydrogen embrittlement is evidenced by different failure pressure values between He and H_2.

2.2 Tensile tests

In the present study, tensile tests were performed in the available range [10^{-4}-10^{-1} s^{-1}]. The tensile curves are presented in Figure 3.

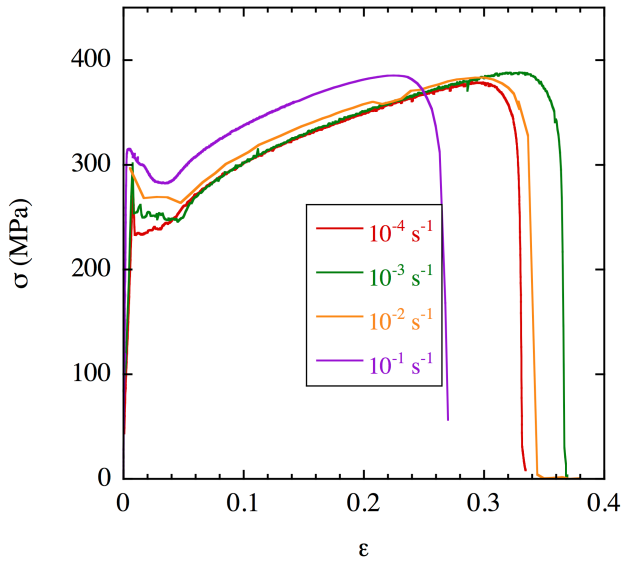

Figure 3. Experimental tensile curves.

In the range [10^{-4}-10^{-2} s^{-1}], the material can be considered non-strain rate dependent, except the Lüders phenomena at the very beginning of the hardening curve, which was neglected in the present work. For larger applied $\dot{\varepsilon}$, strain-rate sensitivity is evidenced, consistently with literature [22]; it is worth noting that in the whole investigated range, the applied strain rate does not affect the ultimate stress value..

In the following, the material is considered as elastic-plastic in the FE simulations of the disk bulging for sake of simplicity. Only standard plasticity is used, even if promising results on hydrogen concentration have been obtained in recent works using strain-gradient plasticity [23] in a small-scale yielding configuration. The influence of hydrogen on mechanical behavior was not considered.

However attention is paid to the strain-rate distribution encountered in the zone of interest during bulging under various applied pressure rates (see below Figure 5), and the influence of yield stress is considered through sensitivity analysis of the results (see section 5.2).

Isotropic hardening was described by a Voce-type hardening law:

$$\sigma_Y = \sigma_0 + R_{sat}\,(1 - e^{-C\varepsilon_p}) \tag{1}$$

where ε_p is the equivalent plastic strain. From the tensile curves corresponding to the non-rate dependent sensitivity range in Figure 1, the following set of parameters was identified: σ_0=232 MPa, R_{sat}=550 MPa and C=1.4.

Two other σ_0 values, respectively equal to 202 and 260 MPa were also used, corresponding to a 25% global variation, for purpose of sensitivity analysis.

Isotropic elasticity was described with Young modulus E=210 GPa and the Poisson ratio ν=0.3.

3 2D axisymmetric simulations with isotropic material behavior

2D axisymmetric computations of the disk bulging were made with 11600 bilinear elements, for each experimental values of $\dot{P}$ (from 3.10^{-3} to 25 MPa/s). Computations were stopped when the applied pressure reached the experimental value of the hydrogen-assisted failure pressure P_F.

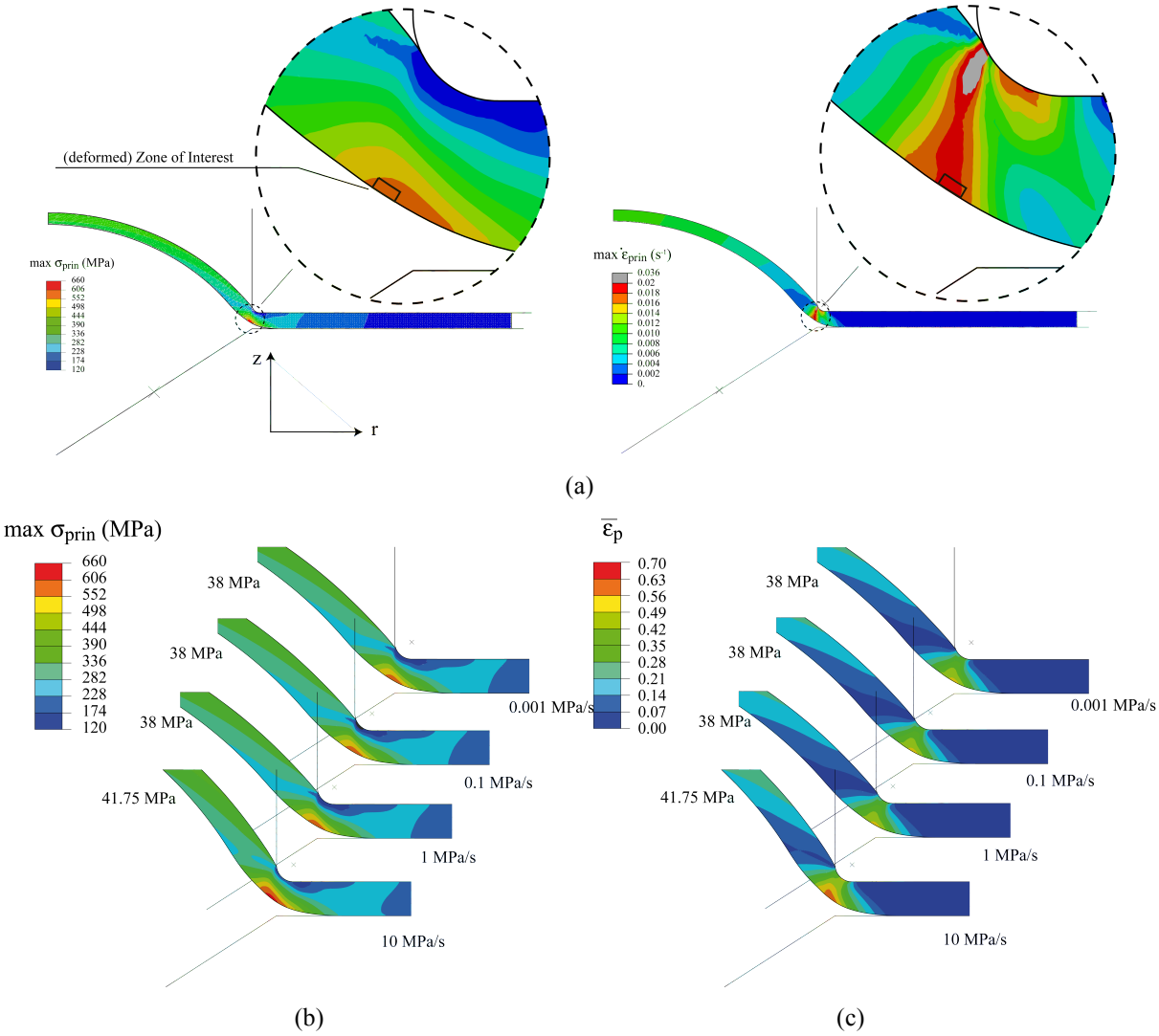

Figure 4. (a) Example of deformed disk with enlarged view showing the Zone of Interest (P=38 MPa and $\dot{P}$=1 MPa/s), and the maximal principal stress and maximal strain rate repartitions. Maps of simulated (b) maximal principal stress, (c) equivalent plastic strain at the experimental P_F values for different applied $\dot{P}$.

Figure 4 shows typical maps of mechanical fields at the end of the calculations. Figure 4a shows in the whole disk the distribution of the maximum principal stress and of the strain rate for $\dot{P}$=1 MPa/s (P_F=38 MPa), with an enlarged view of the ZoI for fracture. In all cases the highest stress and strain values are localized in the ZoI.

Due to elastoplasticity assumption, stress and strain fields do not depend on $\dot{P}$. The local values at the end of the calculation, however, vary with $\dot{P}$ because of the different final values of P_F, as illustrated by Figure 4b-c. In the ZoI, for all $\dot{P}$ values, the average equivalent plastic strain rate $\dot{\varepsilon}_p$ remains almost constant during the test (see Figure 5), with values varying

typically from 10^{-5} s^{-1} (for $\dot{P}$=10^{-3} MPa/s) to 10^{-1} s^{-1} (for $\dot{P}$=10 MPa/s). As a consequence, non-rate material sensitivity is a reasonable assumption for pressure rates lower than 1 MPa/s.

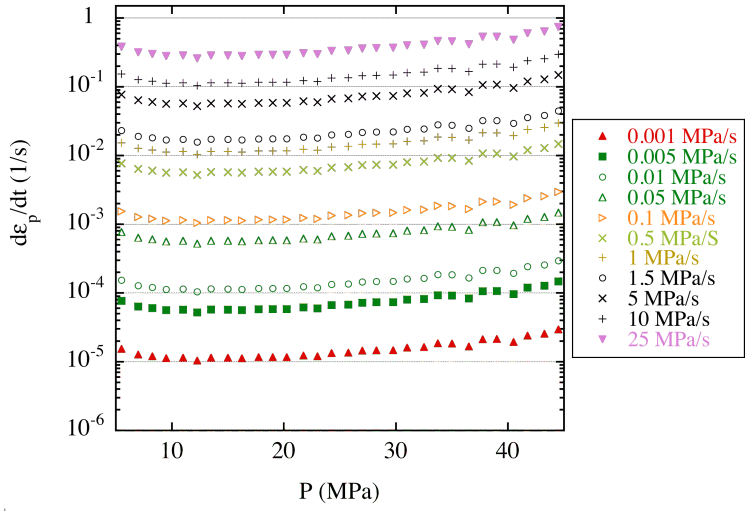

Figure 5. Variation of the average equivalent plastic strain rate in the ZoI for different applied pressures rate.

4 Hydrogen transport modeling

The details of formulations of hydrogen transport in the framework of continuum mechanics, accounting for instantaneous or transient trapping by dislocations, can be found elsewhere, together with the related numerical implementation procedures [13,24,25]. Only the main features are reported here.

4.1 Analytical formulations of hydrogen transport and trapping

Considering the total hydrogen concentration C as the sum of a diffusive C_L ($C_L = N_L\theta_L$) and a trapped C_T ($C_T = N_T\theta_T$) part, related to their respective site density (N_L, N_T) and occupancy (θ_L, θ_T), the hydrogen transport resulting from mass conservation is described by the equation

$$\frac{\partial C}{\partial t} = \boldsymbol{\nabla} \cdot \boldsymbol{\varphi} \tag{2}$$

where the hydrogen flux $\boldsymbol{\varphi}$ accounting for the hydrostatic pressure P_H can be written as

$$\boldsymbol{\varphi} = -D_L \boldsymbol{\nabla} C_L - D_L C_L \frac{V_H}{RT} \boldsymbol{\nabla} P_H \tag{3}$$

which leads to

$$\frac{\partial C_L}{\partial t} + \theta_T \frac{\partial N_T}{\partial t} + N_T \frac{\partial \theta_T}{\partial t} + \boldsymbol{\nabla}.\left(-D_L \boldsymbol{\nabla} C_L - D_L C_L \frac{V_H}{RT} \boldsymbol{\nabla} P_H\right) = 0 \tag{4}$$

The following values were used for iron: D_L=1.27×10^{-8} m^2/s, N_L=8.46×10^{28} site/m^3, and V_H=2×10^{-6} m^3/mol [1,8,26]. Trapping by dislocations is described by the phenomenological relationship between N_T and the equivalent plastic strain ε_p as proposed in literature [8,27]:

$$\log\ N_T = 23.26 - 2.33\exp^{-5.5\varepsilon_p} \tag{5}$$

Due to large plastic strains reached in the disk area where hydrogen-assisted failure is triggered, trapping by dislocations is assumed prominent, and no other traps are considered in this work.

When assuming $\theta_L \ll 1$, the trap occupancy evolution with time is described with the McNabb and Foster equation [28]

$$\frac{\partial \theta_T}{\partial t} = p\theta_L(1-\theta_T) - k\,\theta_T \tag{6}$$

where p and k are material-dependent parameters, respectively equal to 2.13×10^{6} s^{-1} and 5.63×10^{-3} s^{-1} [12,29].

For instantaneous trapping ($\partial\theta_T/\partial t = 0$), equation (6) provides a direct relationship between θ_L and θ_T (following Orianis work [11]) and equation (4) becomes

$$\frac{C_T(1-\theta_T)+C_L}{C_L}\frac{\partial C_L}{\partial t} + \boldsymbol{\nabla}.\left(-D_L\boldsymbol{\nabla}C_L - D_L C_L\frac{V_H}{RT}\boldsymbol{\nabla}P_H\right) + \theta_T\frac{dN_T}{d\varepsilon_p}\dot{\varepsilon}_p = 0 \tag{7}$$

which was implemented in Abaqus code using UMAT and UMATHT procedures [24,25].

For transient trapping, numerical resolution was made in Abaqus after implementation of an analytical approximation of the solution of Equation (6), as shown in a recent paper [13].

All implementations related to hydrogen transport permitted the simultaneous resolution of the mechanical and diffusion problems. This is of special importance in the context of disk bulging simulations, in which mechanical and diffusion related fields evolve simultaneously.

4.2 Hydrogen boundary conditions

To simulate the disk bulging under increasing hydrogen gas pressure, the initial-boundary value problem is solved from the simultaneous application of a constant pressure rise rate $\dot{P}$ and a hydrogen concentration C_{L0} on the lower disk face submitted to the gas pressure. Assuming a Langmuir isotherm formulation, C_{L0} is linked to the applied pressure by the relationship

$$\frac{C_{L0}}{C_0} = \lambda\frac{K\sqrt{P}}{1+K\sqrt{P}} \tag{8}$$

where K is a material parameter equal to 1.27×10^{-2} Pa$^{-1/2}$ [2,30]. λ is set so that for P=1 atm, $C_{L0} = C_0$, leading to

$$\lambda = 1 + \frac{1}{10^{2.5}K} \tag{9}$$

The value of C_0 is chosen equal to 2.084×10^{21} atom/m^3, as computed in [8,31] using the following Sivert Law as proposed in [32]

$$C_L = 1.989\times10^{26}\sqrt{P}\exp\left(-\frac{\Delta H_s}{RT}\right) \tag{10}$$

considering ΔH_s=28.6 kJ/mol [26].

5 Finite Element simulations of hydrogen transport during the DPT

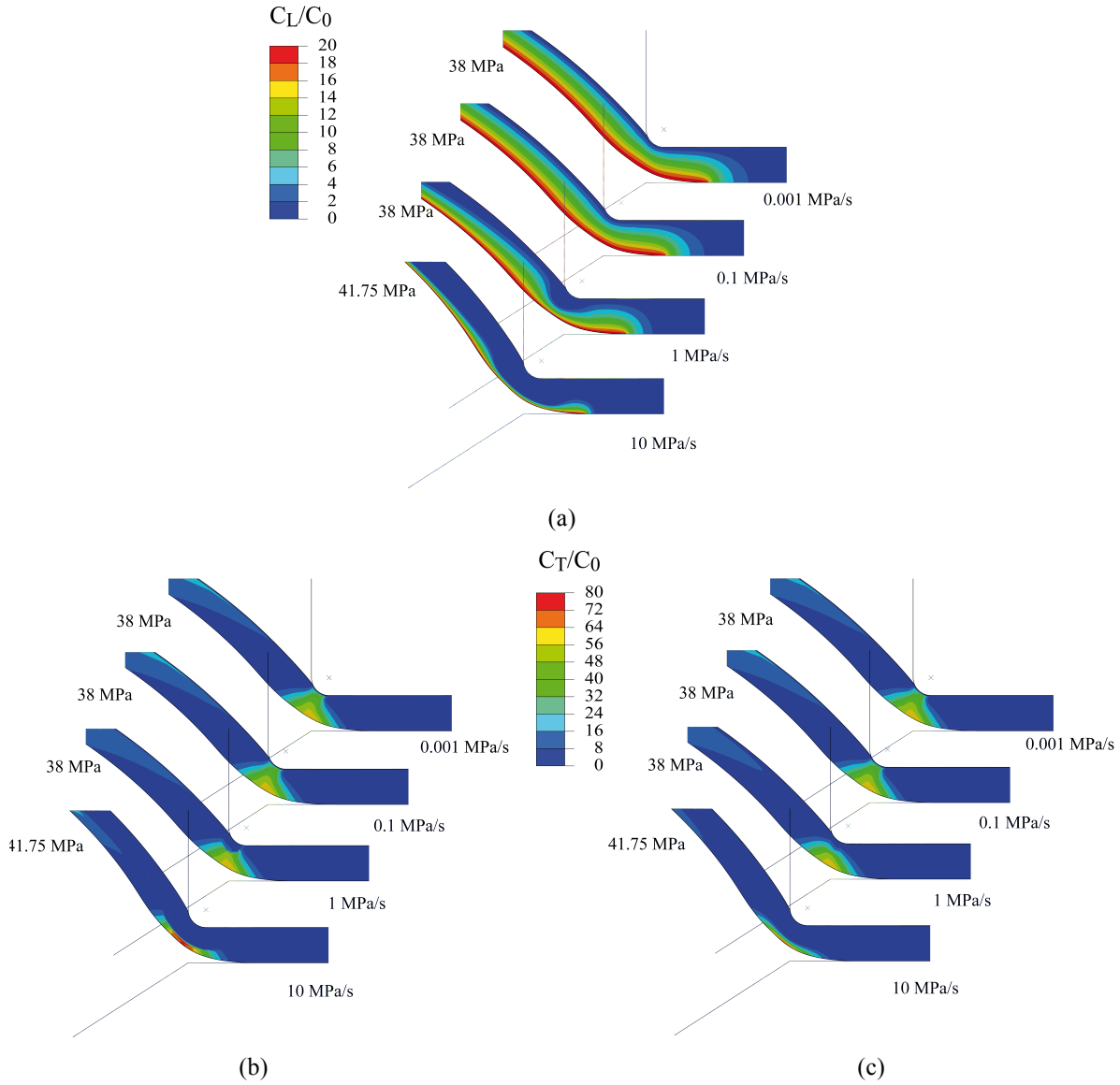

Figure 6. Maps of simulated (a) diffusive and (b) instantaneous or (c) trapped hydrogen concentration in the disks, for different $\dot{P}$ values, at the pressure corresponding to the experimental fracture P_F.

Two simulations have been performed to estimate the hydrogen repartition during the DPT, considering instantaneous or transient trapping.

Figure 6a-b show the diffusive and trapped hydrogen fields computed with instantaneous trapping. As expected, the C_T maps correlate with the ε_p ones, and Figure 6a clearly shows the influence of $\dot{P}$ on the apparent diffusion front through the disk, due to higher trapping in the most deformed areas. For very low $\dot{P}$ values, the C_L concentration is not disturbed by the plastic strain, showing the apparent diffusion characteristic time is far greater than the deformation one, while for very high $\dot{P}$ values, hydrogen transport is not fast enough to completely enter through the disk before its deformation. Between the two, as illustrated for $\dot{P}$=1 MPa/s, the trapping process slows down the hydrogen transport front in the zone of interest, where the plastic strain is highest.

The calculations with transient trapping showed negligible effect on C_L maps, while sensible trapping reduction is visible on C_T maps (compare Figure 6b and c).

5.1 Identification of an hydrogen-dependent critical principal stress for fracture initiation

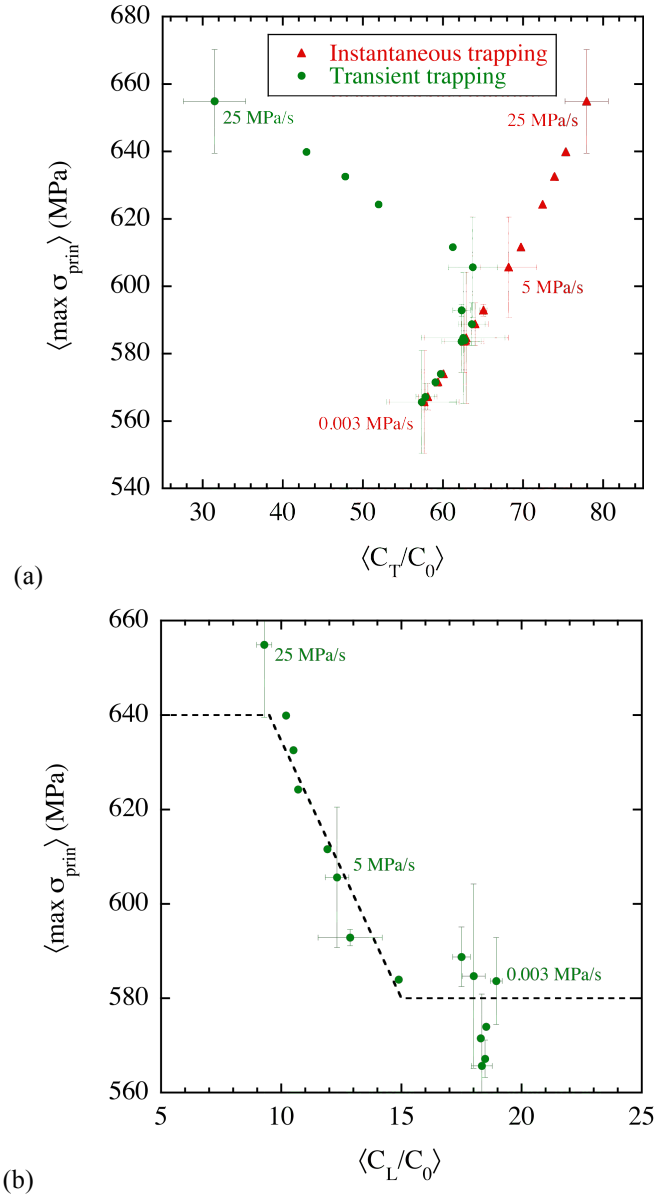

Figure 7. Average maximal principal stress in the ZoI evolution with (a) the average trapped hydrogen concentration considering an instantaneous or a transient trapping and (b) the average diffusive hydrogen concentration considering a transient trapping. On graph (b) is also plotted the evolution of failure stress with the diffusible hydrogen concentration (see equation (11)).

From each simulation, the average values of the maximum principal stress $\langle \max \sigma_{Prin} \rangle$, the diffusive $\langle C_L \rangle$ and the total $\langle C_T \rangle$ hydrogen concentrations have been computed in the ZoI for the P_F values (defined in Figure 4a). Figure 7 presents the evolution of $\langle \max \sigma_{Prin} \rangle$ vs $\langle C_T \rangle$ and $\langle C_L \rangle$, considering an instantaneous or a transient trapping.

Comparing transient and instantaneous trapping results on Figure 7a, it can be seen that $\langle \max \sigma_{Prin} \rangle$ increases with $\langle C_T \rangle$ when trapping is supposed instantaneous whereas it decreases for a transient one. As the material is non-rate dependent, instantaneous trapped hydrogen - directly related to the plastic strain - increases with the applied pressure, whatever the applied

pressure rate. As a consequence, the predicted instantaneous trapped hydrogen is probably overestimated, especially for the highest pressure rate. Concerning diffuse hydrogen, both assumptions on trapping lead to the same tendency, i.e. decrease of $\langle \max \sigma_{Prin} \rangle$ with $\langle C_L \rangle$, which is consistent with an hydrogen embrittlement process.

Last, it is worth noting that for $\dot{P}$ values lower than few MPa/s, the Oriani's assumption (instantaneous trapping) is sufficient to describe the hydrogen transport and trapping in the disk; for higher values of $\dot{P}$, a kinetic trapping model is needed.

The evolution of $\langle \max \sigma_{Prin} \rangle$ with $\langle C_L \rangle$ in the ZoI considering transient trapping (see Figure 7b) is therefore proposed as a hydrogen-dependent stress criterion for initiation of embrittlement. From these numerical results, the evolution of failure stress with diffusible hydrogen concentration is modeled using the very simple following formulation

$$\begin{cases} C_L < 9.5C_0, \;\; \sigma_R = 640 \text{ MPa} \\ 9.5C_0 \leq C_L \leq 15C_0, \;\; \sigma_R = -11.091 \dfrac{C_L}{C_0} + 745.97 \text{ MPa} \\ 15C_0 < C_L, \;\; \sigma_R = 580 \text{ MPa} \end{cases} \tag{11}$$

which is illustrated by the dashed line on Figure 7b.

This phenomenological approach may be roughly interpreted as a HEDE mechanism (Hydrogen Enhanced Decohesion) of hydrogen embrittlement, even if several other concomitant process may occur at the microstructural scale, such as HELP (Hydrogen Enhanced Localized Plasticity) [33,34], which is not considered here as the mechanical behavior does not depend on hydrogen here.

5.2 Influence of the mechanical behavior on the $\sigma_R(C_L)$ curve

Figure 8 presents the evolution of the results presented in Figure 7, when the yield stress is modified to account for strengthening or softening material response.

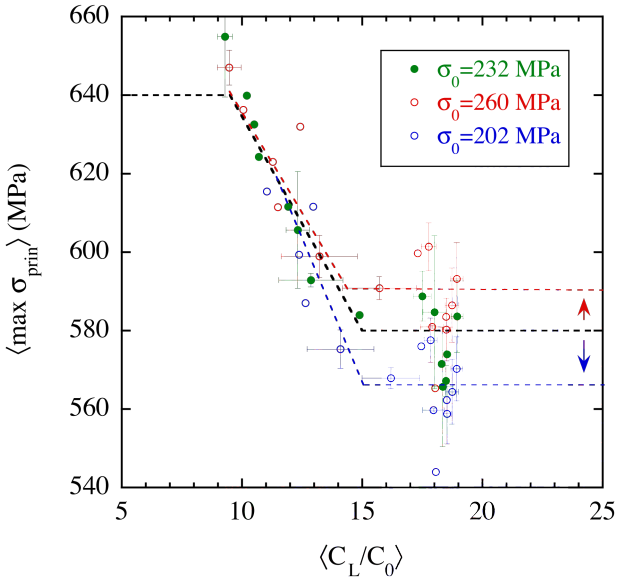

Figure 8. Influence of the yield stress on the evolution of the failure stress with the diffusible hydrogen concentration.

As it can be seen, the influence of the yield stress on the $\sigma_R(C_L)$ evolution is negligible. While the upper σ_R plateau remains unchanged (at 640 MPa), the lower one is decreased around 565 MPa (for $\sigma_0 = 202$ MPa) or increased to 590 ($\sigma_0 = 260$ MPa), i.e. 2-3%. As a consequence, in the frame of the present study modeling assumptions, strengthening or

softening behavior compared to the reference one has a relatively low effect on the $\sigma_R(C_L)$ curve, and is not considered in the following.

6 Application at the polycrystal scale

In the above simulations, spatial variations of the different fields are very smooth inside and around the ZoI, due to the assumption of macroscopic material homogeneity. To estimate the effect of the polycrystalline nature of the material and of its mechanical anisotropy, refined 3D simulations were made using crystal plasticity.

6.1 Crystalline elastoplasticity:

The anisotropic elasticity was described through the elastic constants: C_{11}=201923 MPa, C_{12}=40384 MPa, C_{44}=80769 MPa, computed from Young modulus and Poisson ratio with the standard relationships for cubic symmetry.

The crystal plasticity is described by a classical viscous formulation [35] for numerical purpose only. The slip rate $\dot{\gamma}^{\alpha}$ on the α^{th} slip system is related to the resolved shear stress τ^{α} by a power-law relationship

$$\dot{\gamma}^{\alpha} = \dot{a}_0 \left(\frac{\tau^{\alpha}}{\tau_c^{\alpha}}\right) \left|\frac{\tau^{\alpha}}{\tau_c^{\alpha}}\right|^{n-1}. \tag{12}$$

τ_c^{α} is the critical resolved shear stress on the α^{th} slip system, $\dot{a}_0$ is a reference strain rate, and n the regularization viscous exponent, chosen high enough to avoid viscous effects. The temporal evolution of τ_c^{α} with the slip evolution on all the slip system is so that [36]

$$\dot{\tau}_c^{\alpha} = \sum_{\beta} h_{\alpha\beta}\dot{\gamma}^{\beta}, \tag{13}$$

$h_{\alpha\alpha}$ represent the self-hardening and $h_{\alpha\beta,\alpha\neq\beta} = q h_{\alpha\alpha}$ the latent one, with

$$h_{\alpha\alpha} = h_0 sech^2 \left|\frac{h_0\gamma}{\tau_s - \tau_0}\right|, \tag{14}$$

$\gamma = \sum_{\alpha}\int_0^t |\dot{\gamma}^{\alpha}| dt$ represents the cumulated shear strain. h_0, τ_0 and τ_s are material parameters, respectively corresponding respectively to the initial hardening rate, the initial and the saturated critical resolved shear stress.

This behavior was implemented in Abaqus through the UMAT developed by Huang [37,38] which has been modify for the purpose of this study [15,24].

Only the 12 slip systems $\{110\}\langle 111\rangle$ for bcc structures were considered in the present study for sake of simplicity.

The h_0, τ_0 and τ_s parameters were identified by inverse method, by best fit of the average simulated response of a cubic 200 grains polycrystal submitted to a tensile test, with the Voce-type hardening law based curve. Uniform mixed-orthogonal (or block) conditions have been defined to model periodicity [39]. Grain orientations were defined by an ORIENT User Subroutine [40], using random sets of Euler angles $(\varphi_1, \Phi, \varphi_2)$, assuming an overall isotropic texture. The resulting set of parameters was used: h_0=100 MPa, τ_0=110 MPa and τ_s=550 MPa (using $q = 1.1$). As a compromise between computational time and non-viscous effects, n has been chosen equal to 20. To avoid spurious effects due to local strain rate

evolutions under viscous formulation, the value of $\dot{a}_0$ has been adapted to keep constant the ratio between the local average strain rate and $\dot{a}_0$, given $\dot{a}_0$=10^{-3} s^{-1} for a local strain rate of 10^{-5} s^{-1}.

6.2 Effect of crystalline anisotropy on mechanical and hydrogen fields

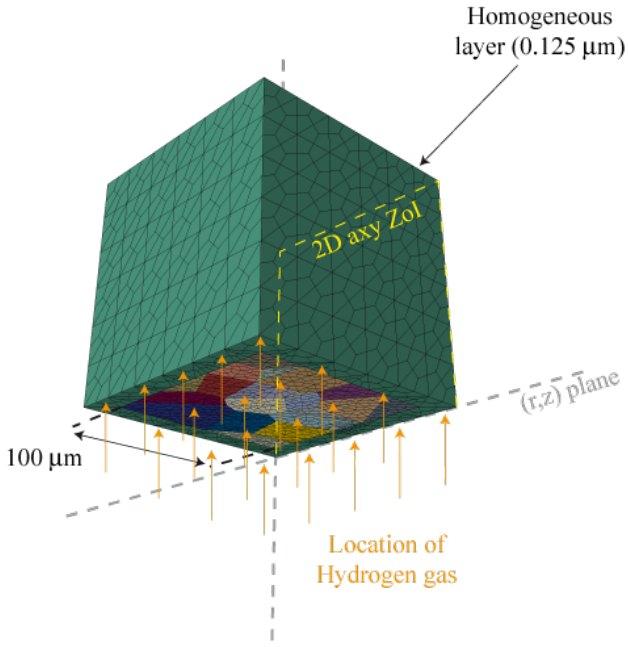

Figure 9. Polycristal setup; the (r, z) plane corresponds to the axysimetric computations (see Figure 4a).

A 100 grains cubic polycristal has been considered the ZoI, using Neper software [41] to generate a Voronoi tessellation. It was embedded, except on its lower face in contact with hydrogen gas, in a homogeneous layer to properly transmit the boundary conditions from the above disk macroscopic simulation. The polycristal is shown on Figure 9. Its size is 100^3 µm^3, while the homogeneous layer thickness is 12.75 µm.

The polycrystal was meshed using 57236 hexahedral elements, and an overall isotropic texture made of a $(\varphi_1, \Phi, \varphi_2)$ Euler angles random set was generated and set constant for all of the computations.

Boundary conditions have been set using a python script for a submodeling-like process. For each external node, the polar coordinates are computed to get an equivalent location in the macroscopic 2D-axixymetric model. The evolution of the displacement with time, on that location, is defined by an interpolation of the results obtained on the closest nodes of the 2D-axisymetric model. The same process is made for the diffusive hydrogen concentration, but the boundary condition transfer is limited on the upper and lower faces of the polycristal (z_{max} and z_{min}, see Figure 9); on the other faces, a 0 normal diffusive hydrogen flux is imposed.

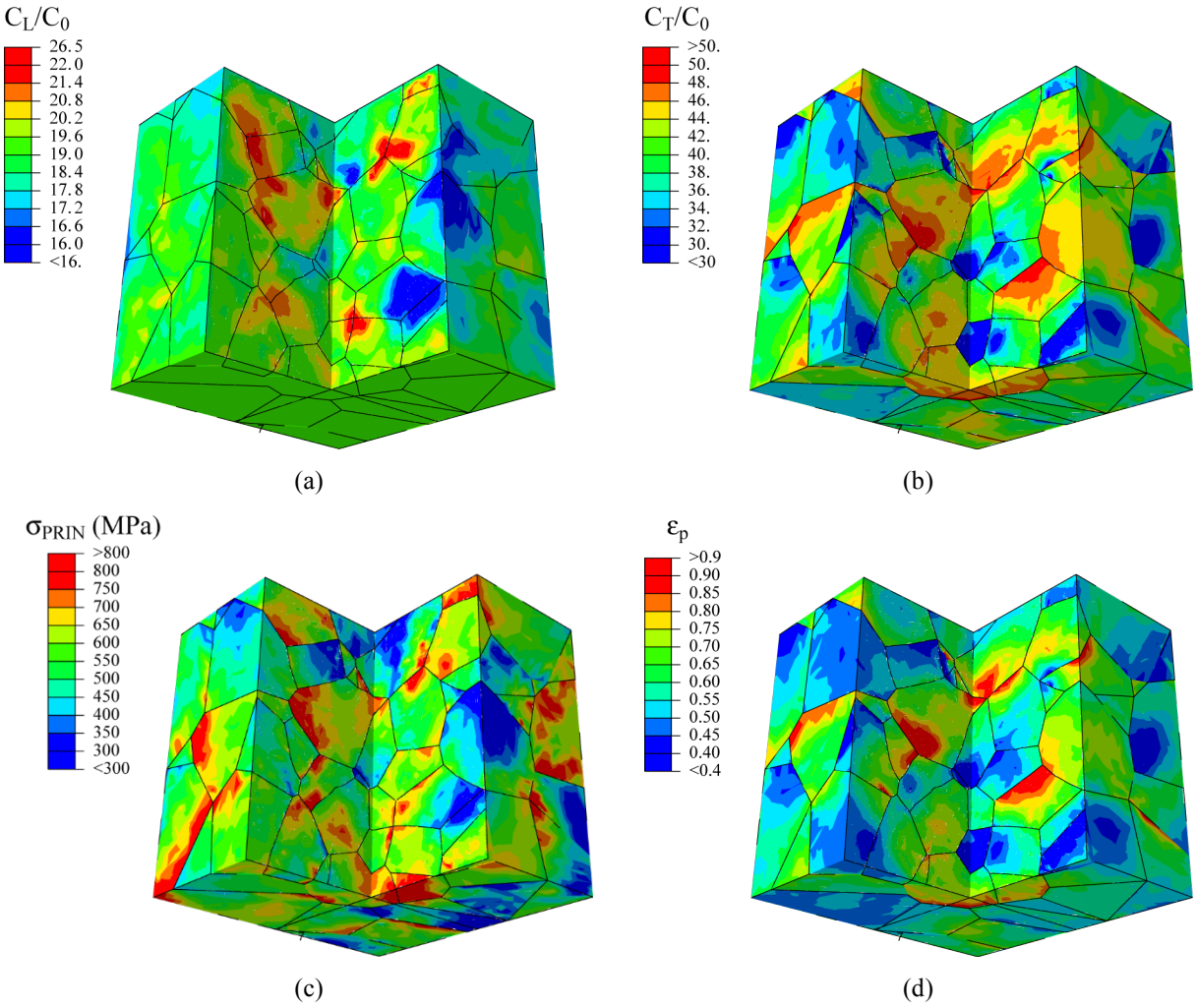

Figure 10. Repartition of (a) C_L/C_0, (b) C_T/C_0, (c) the maximal principal stress and (d) the equivalent plastic strain for $\dot{P} = 0.1\ MPa/s$ and $P = 38\ MPa$,. For the sake of illustration, ¼ of the undeformed polycrystal (see Figure 9) has been removed.

All hydrogen related parameters were the same as for the macroscopic simulations, except the trapped density, which was set as

$$N_T{}^{poly} = 0.57 N_T{}^{homo} \tag{15}$$

where $N_T{}^{poly}$ and $N_T{}^{homo}$ are the trap density at the crystal scale and at the macroscopic one respectively. The value 0.57 is a corrective factor introduced, as a first approximation, to ensure the consistency of the average diffusion and trapping process between a polycrystal and an equivalent homogeneous medium, which was shown in a recent paper [24] not to be quantitatively obtained.

6.3 Effect of crystalline anisotropy on mechanical and hydrogen fields

The different fields in the polycrystal are plotted on Figure 10. As expected, they exhibit heterogeneities induced by the various crystal orientations in the ZoI.

The influence of the mechanical anisotropy on the C_L and maximal principal stress values is shown on Figure 11, for the two extreme applied pressures rates (25 and 0.001 MPa/s). Two computations are considered, using the same mesh: one using polycrystalline plasticity (see Figure 10) and one using homogeneous elastoplasticity. At each mesh Gauss point, the fields

obtained in the two computations are compared, and their ratios are plotted in term of frequency.

Figure 11 compares the distribution of the maximal principal stress and of the diffusive hydrogen concentration throughout the ZoI for two pressure rate values. A significant larger spreading of the results can be noticed, which can reach up 50% for the maximal principal stress, and up 25% for the hydrogen concentration.

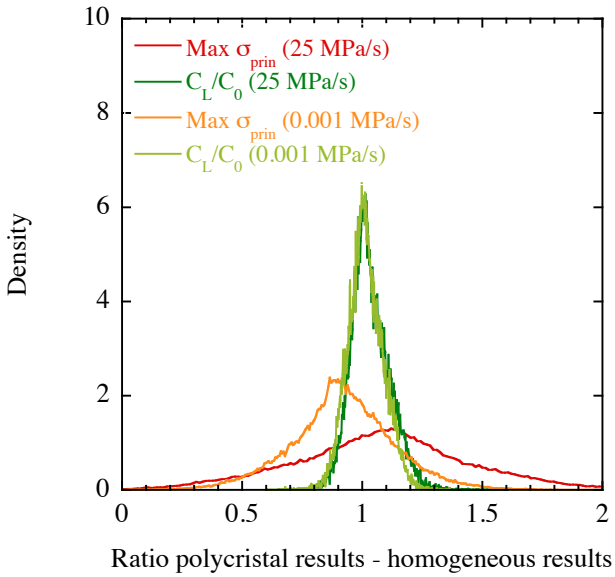

Figure 11. Ratio of the maximal principal stress and diffusive hydrogen in the case of instantaneous trapping for an applied presure rate of 25 MPa/s and 0.001 MPa/s. A ratio equals to 1 means that the mechanical heteorgeneities induced by the polycrystalline features do not affect the considered fields, compared to the 2D axisymetric computation.

As a consequence, the risk of failure (i.e., the probability to get a point with high stress and hydrogen concentration values) may sensibly increase when considering the material mechanical anisotropy. Using equation (11) from Figure 7b to compute the failure stress on each Gauss point of the polycrystalline aggregate from its corresponding C_L value permit to estimate the induced dispersion (compared to the macroscopic results of section 5.1) of the failure stress for various applied pressure rate (Figure 12).

For low applied pressure rate, the C_L values in the polycrystal leads to a failure stress close to its minimal value, following equation (11). For high $\dot{P}$ values, which induce lower C_L values, huge variations of the failure stress are found throughout the polycrystal Gauss Points.

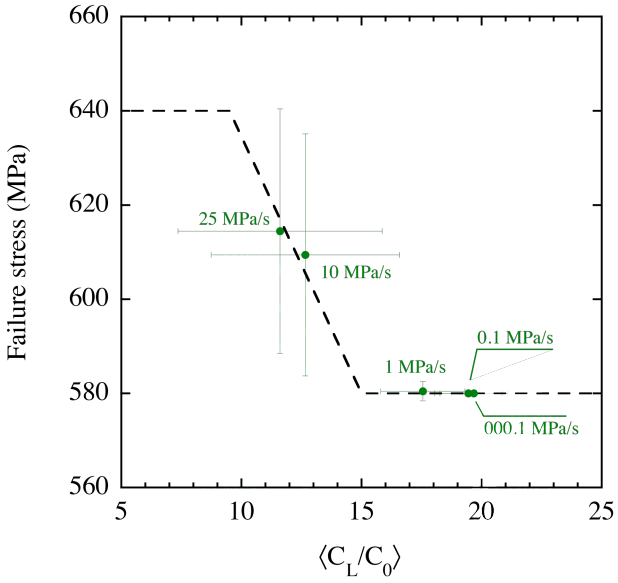

Figure 12. Failure stress variation with the hydorgen content in the polycrystal from the submodeling approach. The dashed black line represent the phenomenological formulation given on equation (11) (see Figure 7b).

Conclusions

In this study, FE simulation of the disk bulging under hydrogen pressure up to fracture initiation by HE has been performed at the macroscopic scale under isotropic elastoplasticity, with submodelling with 3D polycrystalline aggregate in the zone of interest for fracture.

The simulation permits to solve simultaneously the mechanical and diffusion initial boundary value problems, based on the development and implantation of user procedures and python scripts in FE Abaqus code. Hydrogen transport involved phenomenological accounting of lattice diffusion and trapping by dislocations, considering instantaneous or transient trapping.

The results show the capacity of the simulations to evidence the effect of the applied pressure rate on the apparent hydrogen diffusion front in the plastically deformed areas, as a result of the competition between diffusion and deformation rates.

The experimental values of pressure fracture under hydrogen for various applied pressure rates obtained by DPT on Armco iron have been used to identity by inverse method a hydrogen-dependent critical stress for HE in the zone of interest depending on the average local diffusive hydrogen concentration. To obtain a decrease of the average maximal principal stress with the increase of the trapped hydrogen concentration, consistent with an expected HE process, transient trapping was shown to be more relevant than the Oriani's assumption of instantaneous trapping.

The choice of diffusive or trapped hydrogen as the driving relevant parameter of embrittlement process is still an open question, far beyond this study. Nevertheless, numerical tools such as the ones used in the present paper are useful for sensitivity studies, provided realistic data. Further work is needed to improve the description of the DPT and/or the hydrogen effects in the implemented constitutive laws.

Submodelling of the zone of interest by a polycrystalline aggregate obeying crystal plasticity permitted to estimate the dispersion induced by the crystal anisotropy and the consequence on the statistical analysis of the risk of failure by HE. This is a first step towards accounting microstructural parameters and hydrogen-material interactions mechanisms in a multi-scale approach, which needs further developments and experimental validations..

Acknowledgements.

The authors thank Dr A. Hocini for the experimental tensile tests.

References

[1] Krom AHM, Koers RWJ, Bakker AD. Hydrogen transport near a blunting crack tip. J Mech Phys Solids 1999;47:971–92. doi:http://dx.doi.org/10.1016/S0022-5096(98)00064-7.

[2] Charles Y, Gaspérini M, Disashi J, Jouinot P. Numerical modeling of the Disk Pressure Test up to failure under gaseous hydrogen. J Mater Process Technol 2012;212:1761–70. doi:10.1016/j.jmatprotec.2012.03.022.

[3] ISO 11114-4. Transportable gas cylinders – compatibility of cylinder and valve materials with gas contents – part 4: test methods for selecting metallic materials resistant to hydrogen embrittlement., 2005.

[4] French standard NF E 29 732. Gas Containers. Cylinders and Containers for Compressed Hydrogen. Test Method for Selecting Construction Materials., 1990.

[5] Tiegel MC, Martin ML, Lehmberg AK, Deutges M, Borchers C, Kirchheim R. Crack and blister initiation and growth in purified iron due to hydrogen loading. Acta Mater 2016;115:24–34. doi:10.1016/j.actamat.2016.05.034.

[6] Ayadi S, Charles Y, Gaspérini M, Caron Lemaire I, Da Silva Botelho T. Effect of loading mode on blistering in iron submitted to plastic prestrain before hydrogen cathodic charging. Int J Hydrog Energy 2017;42:10555–67. doi:10.1016/j.ijhydene.2017.02.048.

[7] Krom AHM, Bakker AD. Hydrogen trapping models in steel. Metall Mater Trans B 2000;31:1475–82. doi:10.1007/s11663-000-0032-0.

[8] Sofronis P, McMeeking RM. Numerical analysis of hydrogen transport near a blunting crack tip. J Mech Phys Solids 1989;37:317–50. doi:10.1016/0022-5096(89)90002-1.

[9] Ardon K. Analyse expérimentale et numérique de l'essai de disque de rupture : Cas de l'acier 35CD4 testé sous hydrogène gazeux. Université Paris 13, Sorbonne Paris Cité, 2015.

[10] Ardon K, Charles Y, Gaspérini M, Sallais D, Furtado J, Barbier F. Experimental and numerical analysis of the Disk Pressure Test for an AISI 4135 steel. Steely Hydrogen, Ghent, Belgium: American Institute of Physics; 2013, pp. 477–87.

[11] Oriani RA. The diffusion and trapping of hydrogen in steel. Acta Metall 1970;18:147–57. doi:10.1016/0001-6160(70)90078-7.

[12] Hurley C, Martin F, Marchetti L, Chêne J, Blanc C, Andrieu E. Numerical modeling of thermal desorption mass spectroscopy (TDS) for the study of hydrogen diffusion and trapping interactions in metals. Int J Hydrog Energy 2015;40:3402–14. doi:10.1016/j.ijhydene.2015.01.001.

[13] Benannoune S, Charles Y, Mougenot J, Gaspérini M. Numerical simulation of the transient hydrogen trapping process using an analytical approximation of the McNabb and Foster equation. Int J Hydrog Energy 2018;43:9083–93. doi:10.1016/j.ijhydene.2018.03.179.

[14] Benannoune S, Charles Y, Mougenot J, Gaspérini M, De Temmerman G. Numerical simulation by finite element modelling of diffusion and transient hydrogen trapping processes in plasma facing components. Nucl Mat Ener 2019;19:42–6. doi:10.1016/j.nme.2019.01.023.

[15] Charles Y, Gaspérini M, Ardon K, Ayadi S, Benannoune S, Mougenot J. Adaptation

of hydrogen transport models at the polycrystal scale and application to the U-bend test. Procedia Struct Integrity 2018;13:896–901. doi:10.1016/j.prostr.2018.12.169.
[16] Ardon K, Charles Y, Gaspérini M, Furtado J. A Numerical and Experimental Study of the Disk Pressure Test. vol. 6B, ASME; 2013, pp. V06BT06A015–5. doi:10.1115/PVP2013-97433.
[17] Fidelle JP, Arnould-Laurent R. The Embedded Disk Pressure Test (DPT): A Sensitive Technique to Investigate Materials Embrittlement. In: Latanison RM, Pickens JR, editors. Atomistics of Fracture, Springer Science & Business Media; 2012.
[18] Barthélémy H. Effects of pressure and purity on the hydrogen embrittlement of steels. Int J Hydrog Energy 2011;36:2750–8. doi:10.1016/j.ijhydene.2010.05.029.
[19] Kruger J, Yolken HT. Room temperature oxidation of iron at low pressures. Corrosion 1964;20:29t–33t.
[20] Song RH, Pyun S II, Oriani RA. Hydrogen Permeation Through the Passivation Film on Iron by Time-Lag Method. J Electrochem Soc 1990;137:1703–6. doi:10.1149/1.2086773.
[21] Briottet L, Moro I, Lemoine P. Quantifying the hydrogen embrittlement of pipeline steels for safety considerations. Int J Hydrog Energy 2012;37:17616–23. doi:10.1016/j.ijhydene.2012.05.143.
[22] Albertini C, Montagnani M, Pizzinato EV, Rodis A. Comparison of mechanical properties in tension and shear at high strain rate for AISI 316 and Armco iron. Mechanical Behaviour of Materials VI, Pergamon; 1992, pp. 351–6. doi:10.1016/B978-0-08-037890-9.50062-4.
[23] Martínez-Pañeda E, del Busto S, Niordson CF, Betegón C. Strain gradient plasticity modeling of hydrogen diffusion to the crack tip. Int J Hydrog Energy 2016;41:10265–74. doi:10.1016/j.ijhydene.2016.05.014.
[24] Charles Y, Nguyen TH, Gaspérini M. Comparison of hydrogen transport through pre-deformed synthetic polycrystals and homogeneous samples by finite element analysis. Int J Hydrog Energy 2017;42:20336–50. doi:10.1016/j.ijhydene.2017.06.016.
[25] Charles Y, Nguyen TH, Gaspérini M. FE simulation of the influence of plastic strain on hydrogen distribution during an U-bend test. Int J Mech Sci 2017;120:214–24. doi:10.1016/j.ijmecsci.2016.11.017.
[26] Hirth JP. Effects of hydrogen on the properties of iron and steel. Met Trans A 1980;11:861–90. doi:10.1007/BF02654700.
[27] Kumnick AJ, Johnson HH. Deep trapping states for hydrogen in deformed iron. Acta Metall 1980;28:33–9. doi:10.1016/0001-6160(80)90038-3.
[28] McNabb A, Foster PK. A new analysis of the diffusion of hydrogen in iron and ferritic steels. Trans Metall Soc AIME 1963;227:618–27.
[29] Turnbull A, Hutchings RB, Ferriss DH. Modelling of thermal desorption of hydrogen from metals. Mater Sci Eng A 1997;238:317–28. doi:10.1016/S0921-5093(97)00426-7.
[30] Nelson HG, Stein JE. Gas-phase hydrogen permeation through alpha iron, 4130 steel, and 304 stainless steel from less than l00°C to near 600°C. NASA; 1973.
[31] Taha A, Sofronis P. A micromechanics approach to the study of hydrogen transport and embrittlement. Eng Frac Mech 2001;68:803–37. doi:http://dx.doi.org/10.1016/S0013-7944(00)00126-0.
[32] Johnson HH. Hydrogen gas embrittlement. In: Thompson AW, Bernstein IM, editors. 7th International conference on the effects of hydrogen on materials properties and selection and structural design, Champion, Pennsylvanie, United State: Cornell Univ.,

Ithaca, N.Y. (USA); 1974, pp. 35–49.
[33] Djukic MB, Sijacki Zeravcic V, Bakic GM, Sedmak A, Rajicic B. Hydrogen damage of steels: A case study and hydrogen embrittlement model. Eng Fail Anal 2015;58:485–98. doi:10.1016/j.engfailanal.2015.05.017.
[34] Gerberich WW, Stauffer DD, Sofronis P. A coexistent view of hydrogen effects on mechanical behavior of crystals: HELP and HEDE. In: Somerday BP, Sofronis P, Jones R, editors. 2008 International Hydrogen Conference, 2009, pp. 38–45.
[35] Asaro RJ. Micromechanics of crystals and polycrystals. Adv Appl Mech 1983;23:1–115. doi:10.1016/S0065-2156(08)70242-4.
[36] Peirce D, Asaro RJ, Needleman A. An analysis of nonuniform and localized deformation in ductile single crystals. Acta Metall 1982;30:1087–119. doi:10.1016/0001-6160(82)90005-0.
[37] Huang Y. A user-material subroutine incorporating single crystal plasticity in the ABAQUS finite element program, Mech Report 178. Cambridge, Massachusetts: 1991. www.columbia.edu/~jk2079/fem/umat_documentation.pdf
[38] Kysar JW. Addendum to "A user-material subroutine incorporating single crystal plasticity in the ABAQUS finite element program, Mech Report 178." Cambridge, Massachusetts: 1991.
[39] Charles Y, Estevez R, Bréchet Y, Maire E. Modelling the competition between interface debonding and particle fracture using a plastic strain dependent cohesive zone. Eng Frac Mech 2010;77:705–18. doi:10.1016/j.engfracmech.2009.11.012.
[40] Simulia. Abaqus User subroutines reference guide. Dassault Système; 2011.
[41] Quey R, Dawson PR, Barbe F. Large-scale 3D random polycrystals for the finite element method: Generation, meshing and remeshing. Comput Methods Appl Mech Eng 2011;200:1729–45. doi:10.1016/j.cma.2011.01.002.